Effect of porous silicon substrate on structural, mechanical and optical properties of MOCVD and ALD ruthenium oxide nanolayers

Article *in* Applied Surface Science · March 2019

DOI: 10.1016/j.apsusc.2018.12.022

CITATIONS
5

READS
186

10 authors, including:

Eugene Brytavskyi
Odessa National University
29 PUBLICATIONS **35** CITATIONS
SEE PROFILE

Kristina Husekova
Institute of Electrical Engineering Slovak Academy of Sciences
66 PUBLICATIONS **572** CITATIONS
SEE PROFILE

Valerii Myndrul
Adam Mickiewicz University
13 PUBLICATIONS **65** CITATIONS
SEE PROFILE

Mykola Pavlenko
15 PUBLICATIONS **140** CITATIONS
SEE PROFILE

Applied Surface Science 471 (2019) 686–693

Contents lists available at ScienceDirect

Applied Surface Science

journal homepage: www.elsevier.com/locate/apsusc

Full Length Article

Effect of porous silicon substrate on structural, mechanical and optical properties of MOCVD and ALD ruthenium oxide nanolayers

Ievgen Brytavskyi[a], Kristína Hušeková[b], Valerii Myndrul[c], Mykola Pavlenko[c], Emerson Coy[c], Karol Zaleski[c], Dagmar Gregušová[b], Luis Yate[d], Valentyn Smyntyna[a], Igor Iatsunskyi[c,*]

[a] Odessa I.I. Mechnikov National University, 2, Dvoryanskaya Str., Odessa 65082, Ukraine
[b] Institute of Electrical Engineering Slovak Academy of Sciences, Dubravskacesta 9, 841 04 Bratislava, Slovakia
[c] NanoBioMedical Centre, Adam Mickiewicz University, 85 Umultowska Str., 61-614 Poznan, Poland
[d] Surface Analysis and Fabrication Platform, CIC biomaGUNE, Paseo Miramón 182, 20009 Donostia-San Sebastian, Spain

ARTICLE INFO

Keywords:
Porous silicon
Ruthenium oxide
ALD
MOCVD

ABSTRACT

Ruthenium oxide (RuO_2) has received significant attention in recent years for its photocatalytic properties and photoelectrochemical (PEC) performance. In the present research, RuO_2 nanolayers were grown on n-type porous silicon (PSi) by metal organic chemical vapor deposition (MOCVD) and atomic layer deposition (ALD). The morphology, mechanical and optical properties of produced nanostructures were studied by means of scanning electron microscopy (SEM), transmission electron microscopy (TEM), energy dispersive X-ray spectroscopy (EDX), X-ray diffraction (XRD), X-ray photoelectron spectroscopy (XPS), micro-Raman spectroscopy, diffuse reflectance and photoluminescence (PL) spectroscopy. It was shown that that MOCVD gives non-uniform distribution of RuO_2 along the pore and it is deposited mainly in the near-surface of PSi, while distribution of ruthenium obtained by ALD looks conformal over the entire pore. The mean size of RuO_2 nanocrystallites and mechanical stresses were determined by TEM, XRD and Raman spectroscopy. It was demonstrated that samples obtained by ALD demonstrate a good crystallinity, while crystalline phase for samples produced by MOCVD improve with RuO_2 layer thickness increasing. It was established the formation of hydrated RuO_2 during ALD and MOCVD. It was shown that the samples produced by MOCVD have slightly higher electrical conductivity than ALD samples. The average value of energy gap (E_g) for samples prepared by MOCVD depended on the number of injections. RuO_2 nanolayers quenched intrinsic PL from the PSi matrix. The correlation between structural, optical, and mechanical properties of samples produced by MOCVD and ALD was discussed.

1. Introduction

Porous silicon (PSi) – metal oxide (MOx) nanostructures and nanocomposites have a great potential in various applications, such as in photocatalysis [1,2], (bio)sensors [3,4], Li-ion batteries [5], etc. It is possible to tailor physical properties of nanocomposites by coupling PSi with different MOx (e.g. TiO_2, ZnO, Al_2O_3 etc.) [6]. In our previous works, we have shown that some optical parameters, as band gap energy (Eg), refractive index (n) and extinction coefficient (k) could be tuned by varying the thickness of TiO_2 in nanocomposites based on TiO_2/PSi [7], and TiO_2/Si nanopillars [8,9]. This is critically important for development of novel nanocomposites which could be used as effective photoelectrodes in photoelectrochemical (PEC) water splitting or optical sensors [8–10]. Therefore, the improvement of PEC properties of PSi-MOx nanocomposites, which can be achieved by choosing the appropriate MOx, is an important research topic.

Ruthenium oxide (RuO_2) with a rutile phase has received significant attention in recent years for its photocatalytic properties and PEC performance [11–13]. It was shown that incorporation of RuO_2 on $NaTaO_3$ films allowed to achieve a maximum photoelectrochemical hydrogen production of 15.7 mmol h^{-1} g^{-1} with a solar-to-hydrogen (STH) conversion efficiency of 4.29% because of enhanced PEC activity of RuO_2 in the visible region [14]. Authors demonstrated the good photoconversion properties of RuO_2 and it seems that combination of RuO_2 with highly porous materials as PSi enables to develop high-quality material for solar water splitting. Thus, a nanocomposite based on the combination of PSi substrate with RuO_2 seems to be prospective photocatalytic material and requires a systematic investigation of its structural, optical and electrical properties.

Many deposition techniques have been used to fabricate RuO_2 films

* Corresponding author.
E-mail address: igoyat@amu.edu.pl (I. Iatsunskyi).

https://doi.org/10.1016/j.apsusc.2018.12.022
Received 31 July 2018; Received in revised form 21 November 2018; Accepted 3 December 2018
Available online 04 December 2018
0169-4332/

such as a rf-reactive sputtering [15], molecular beam epitaxy (MBE) [16], atomic layer deposition (ALD) [17,18], chemical vapor deposition (CVD) [19], metal organic chemical vapor deposition (MOCVD) [20], and electrochemical deposition [21]. Among all of these techniques, ALD and MOCVD are considered to be the most suitable to deposit thin layers of RuO_2 onto the PSi substrate. Both methods demonstrate good thickness control and conformality of the deposited layer. MOCVD involves the deposition of thin MOx films on a heated substrate using a mixture of gas precursors: a metal organic and an oxidant. This method has the advantages of good conformality and high film uniformity even for non-planar structures. However, the introduction of precursors in ALD occurs in a repeated cycle what allows controlling the thickness of fabricated nanolayers and this method operates at much lower temperatures comparing to MOCVD. To our knowledge, there are no researches comparing physical properties of RuO_2 nanolayers deposited on PSi substrate using these two deposition techniques.

In the present research, a comprehensive study of PSi substrates combined with RuO_2 nanolayer formed by MOCVD and ALD, are presented and discussed in detail. The morphology, phase structure and composition depending on the deposition method were detected by the scanning and transmission electron microscopy (SEM, TEM), XRD, energy dispersive X-ray spectroscopy (EDX), X-ray photoelectron spectroscopy (XPS) and Raman spectroscopy. We revealed that the crystallinity of RuO_2 layers and mechanical stresses at Si-RuO_2 interface depend on the deposition technique. This finding provides a comprehension of morphology evolution during MOCVD and ALD of porous substrates. Optical properties have been also analyzed by means of diffuse reflectance and photoluminescence (PL) spectroscopy. An analysis of the PL spectra revealed the PL quenching due to photogenerated charge carriers separation at the PSi/RuO_2 heterojunction. The results obtained are very promising for the improved use of PSi-RuO_2 structures in photocatalysts, photovoltaic and sensor application.

2. Experimental section

2.1. Preparation of PSi

Initial PSi structures were fabricated by typical metal assisted-chemical etching process (MACE) applied to n-type (1 0 0) 1–10 Ω·cm silicon wafer [22,23]. The wafer was cut into samples with a size of $1.5 \times 1.5\ cm^2$. In the order of removing various contaminations from the surface a standard RCA procedure was performed. After ultrasonication in acetone, water and ethanol for 15 min at each step and degreasing in Piranha solution (98% H_2SO_4/30% H_2O_2 = 3:1, v/v) at room temperature for 30 min the native oxide layer was removed in 5% HF for 10 min. The catalyst in the etching process, represented by Ag layer of thickness 60 nm was deposited on Si pieces via magnetron sputtering. The etching process was conducted in HF/H_2O_2/H_2O = 20/30/80 for 15 min at room temperature. In order to remove the residual Ag inclusions, samples were dipped into HNO_3:H_2O = 1:1 solution for 30 min. At the final step silicon pieces were thoroughly rinsed by deionized water and dried in N_2 flow.

2.2. MOCVD and ALD deposition

RuO_2 films with thickness of 6–28 nm were prepared by using metal-organic chemical vapor deposition (MOCVD) technology in a low-pressure hot-wall quartz reactor and by atomic layer deposition (ALD) technique. For transport of metal-organic precursor to the reactor chamber, the liquid injections of the precursor, dissolved in an appropriate solvent, were employed. This liquid source delivery technology is termed as liquid injection metal-organic chemical vapor deposition (LI MOCVD). Metal-organic precursor bis(2,2,6,6-tetramethyl-3,5-heptanedionato)(1,5-cyclooctadiene) ruthenium, Ru(thd)$_2$(cod), dissolved in a solvent was introduced into the evaporation chamber using electromagnetic micro-valve.

Table 1
MOCVD and ALD parameters of RuO_2 deposition.

Deposition parameter	MOCVD	ALD
Solvent	Isooctane	ethylcyclohexane
Deposition temperature [°C]	290	250 ± 20
Evaporation temperature [°C]	200	160
Pressure [Pa]	266	not constant (depends on the step)
Argon flow rate [sccm]	20	45 (I, II, IV steps)
Oxygen flow rate [sccm]	170	200 (III step)
Oxygen pulse time [s]	Continuously	80 (III step)
Purge time [s]	_	30 (II step), 50 (IV step)
Pressure Ru(thd)2(cod)	–	24 Pa
Pressure O_2	–	105 Pa

Alternatively, the liquid injection MOCVD can be transformed to ALD. The ALD deposition cycle consisted of four steps: (I) multiple injections of the precursor, (II) purge of the reactor by Ar, (III) O_2 introduction, (IV) purge of the reactor by Ar. Deposition conditions for both MOCVD and ALD techniques are given in the Table 1 [18].

All of the indicated parameters were kept constant during both deposition processes. The variations were done only in number of injections (from 60 to 150) for MOCVD and in number ALD cycles (from 50 to 130). Therefore, the only expected difference in sample parameters was the thickness variation due to change of total time of deposition process. Therefore, samples were titled in the following manner: M_N, where M – the deposition method and N – the number of ALD or MOCVD cycles/injections (e.g. ALD_90, MOCVD_150).

The set of three samples was used for each deposition round, which included PSi sample, flat (1 0 0) n-type Si sample with 2 nm native surface SiO_2 layer for X-ray reflectivity (XRR) and resistivity measurements and quartz sample for transmittance measurements.

XRR patterns of the RuO_2 films grown by MOCVD and ALD were measured on flat Si samples. RuO_2 layers were characterized by low-angle X-ray reflectivity measurement between 0.5 and 10 degrees with Bruker D8 DISCOVER diffractometer equipped with an X-ray tube with a rotating Cu anode. The reflectivity curves were analyzed using the software LEPTOS 3.04 provided by Bruker Company (SI, Fig. S1). Theoretical curves were calculated for a simple model comprising the substrate, thin interlayer (~2 nm thick) and RuO_2 layer. Density of both layers changed linearly with depth. Fitting parameters were the thicknesses, the densities of both layers as well as the roughness (root mean square) of the two interfaces and of the surface. Genetic algorithm was used for simultaneous optimization of the variable parameters [24]. Layer densities, layer thickness, and interface roughness were varied in order to obtain the best agreement between the experimental and calculated dependencies. MOCVD grown films showed thickness of 6 nm after 60 precursor injections, 10 nm after 80 precursor injections and 23 nm after 150 precursor injections and surface roughness for these samples was respectively 1 nm, 1.8 nm and 2.4 nm, while ALD grown films appeared to be 18 nm after 50 cycles, 20 nm after 90 cycles and 28 nm thick after 130 cycles with surface roughness respectively 2.8 nm, 4 nm and 2.5 nm (SI, Fig. S1, Table S1). Lower surface roughness of the MOCVD grown films was also observed on SEM images.

2.3. Material characterization and optical measurements

Structural properties of PSi and ALD/MOCVD RuO_2 thin films were investigated by X-ray diffraction (XRD) (PANalytical, X'pert^3 pro-MRD diffractometer) working with a Cu lamp (λ = 1.5418 Å), scanning electron microscopy (SEM) (JEOL, JSM7001F) with an energy dispersive X-ray (EDX) analyzer, transmission electron microscopy (TEM) (JEOL ARM 200F high-resolution transmission electron microscope (200 kV) with EDX analyzer), and Raman scattering (Renishaw

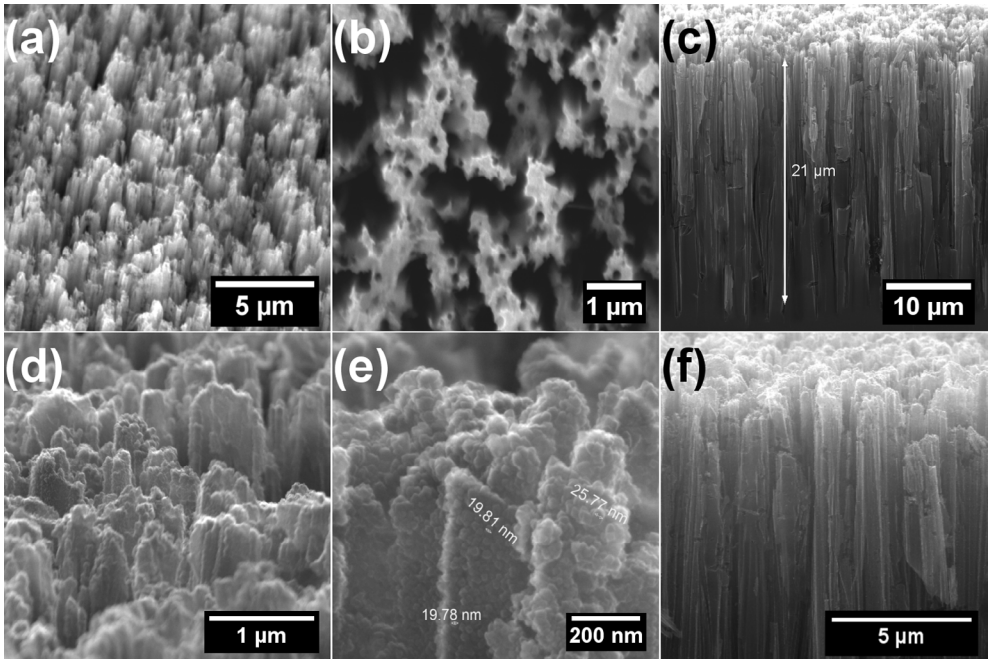

Fig. 1. SEM of PSi surface (a, b) and cross-section (c) before oxide deposition and after RuO_2 layer formation by 130 ALD cycles (d, e, f).

microRaman spectrometer equipped with a confocal microscope (Leica) and laser ($\lambda_{excitation}$ = 514 nm). The cross sections and lamellas for TEM investigations were prepared by Focused Ion Beam (JEOL, JIB-4000). X-ray reflectometry (XRR) measurements were performed Bruker D8 DISCOVER diffractometer equipped with an X-ray tube with a rotating Cu anode. Optical properties of nanocomposites have been studied with UV − vis transmittance (UV − vis spectrophotometer lambda 950 UV/vis/NIR range 300–1100 nm, 1 nm step), reflectance and photoluminescence spectroscopy (OceanOptics spectrometer).

3. Results and discussion

3.1. Morphology and structural properties

Fig. 1a and b display SEM images of PSi surface obtained by MACE. PSi samples show highly textured surface, the irregular columnar structure with shallow micropores (Fig. 1a and b). The average size of macropores is about 1–2 µm and the thickness of of porous layer is approximately 21 µm (Fig. 1c). All samples obtained by both deposition methods have shown conformal coverage of the surface by RuO_2 (Fig. 1d–f, SI Fig. S2). It is clearly seen that the RuO_2 layer has a granular morphology with average grain sizes of 18 nm for ALD samples (Fig. 1d) and 25 nm for MOCVD layers (SI Fig. S2). Cross-sectional SEM images show the infiltration of RuO_2 inside pores (Fig. 1f). In order to estimate the depth of RuO_2 we have also performed TEM/EDX measurements.

Fig. 2a and c show the TEM image of the PSi after the 150 injections of MOCVD and 130 cycles of ALD, respectively. One can observe the thin layer consisting of RuO_2 nanocrystallites, which cover PSi. It is clearly seen that the MOCVD gives non-uniform distribution of ruthenium along the pore and it is deposited mainly in the near-surface of PSi (Fig. 2a), while distribution of ruthenium obtained by ALD looks conformal over the entire pore (Fig. 2c). We may assume that MOCVD processes mainly occur in a thin top-layer of PSi while during the ALD process molecules of precursors penetrate into the pore forming the layer of RuO_2 inside the PSi matrix. This fact is also confirmed by TEM-EDX analysis. Fig. 2b and d indicate the distribution of Ru atoms in PSi. We can notice that Ru atoms are distributed in a thin layer (~2µm) for samples obtained by MOCVD and the full pore coverage for ALD

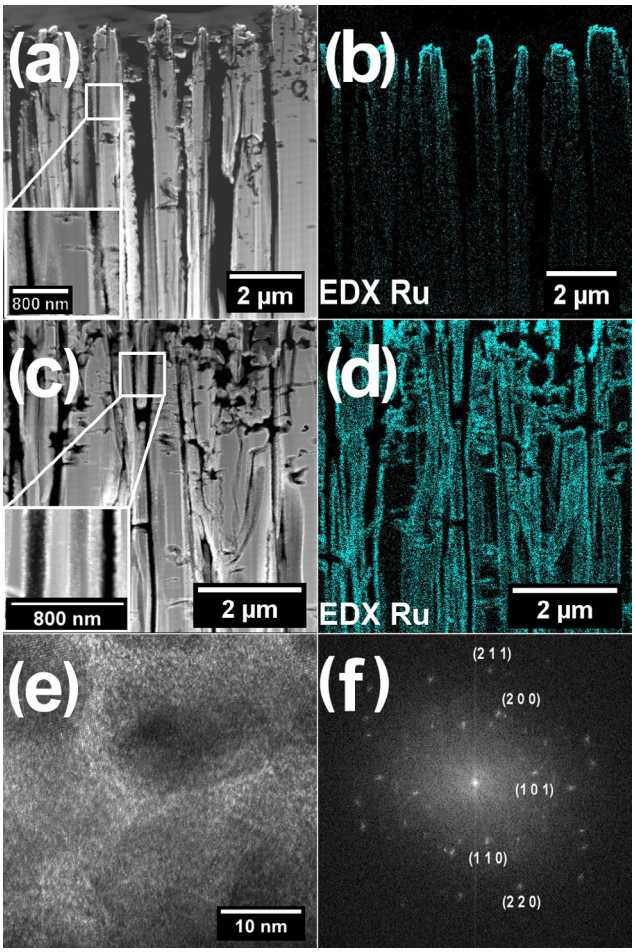

Fig. 2. TEM and EDX images of as-prepared MOCVD (a, b) and ALD (c, d) PSi/RuO_2 nanostructures; (e) the high-resolution TEM of ALD_90 and (f) the FFT image.

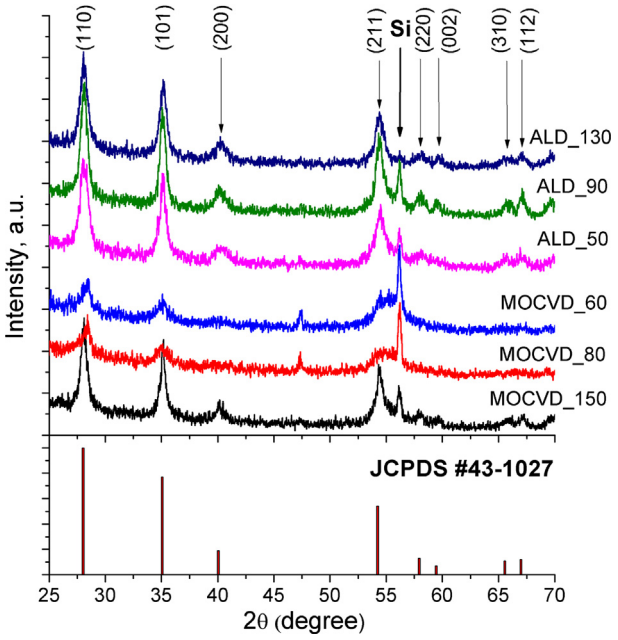

Fig. 3. XRD spectra of MOCVD and ALD PSi/RuO_2 nanostructures.

samples.

In order to investigate the crystallinity of obtained PSi/RuO_2 nanostructures the high-resolution TEM (HR-TEM) measurements were performed. HR-TEM image of the PSi/RuO_2 nanostructure produced by ALD is shown in Fig. 2e. We can observe of polycrystalline structure of RuO_2 (Fig. 2f). Lattice fringes, which are clearly visible in the HR-TEM image indicates the forming of RuO_2 nanocrystallites in the PSi matrix. We estimated the interplane distance of 0.32 nm, 0.26 nm, 0.25 nm, and 0.17 nm for RuO_2 and 0.27 nm, 0.16 nm and 0.13 nm for silicon, respectively. They correspond to the lattice distance of (1 1 0), (1 0 1) and (2 0 0) planes of the rutile RuO_2 and (3 1 1) and (2 0 0) planes of silicon. The average size of RuO_2 nanocrystallites varied from 10 ± 2 nm to 7 ± 4 nm for samples produced by ALD and MOCVD, respectively.

Fig. 3 shows XRD patterns of PSi/RuO_2 nanostructures fabricated by MOCVD and ALD. Measured XRD spectra represent the set of sharp and broad peaks assigned to (1 1 0), (1 0 1), (2 0 0), (2 1 1), (2 2 0), (0 0 2), (3 1 0) and (1 1 2) crystallographic directions corresponding to tetragonal phase of RuO_2 (JCPDS 43-1027). We can observe the improvement of crystalline phase for samples produced by MOCVD with increasing a number of injections, and as a consequence the thickness of RuO_2. However, it is still highly polycrystalline for the sample with the minimum number of MOCVD injections (corresponding to approximately 6 nm). Samples obtained by ALD demonstrate a good crystallinity for all samples.

In order to estimate the average size of nanocrystallites and deformations in PSi/RuO_2 nanostructures the Debye – Scherrer and Williamson – Hall calculations were performed [25]. The average size of RuO_2 nanocrystallites (D) was calculated as: [25]

$$D = \frac{k\lambda}{\beta\cos\theta}, \quad (1)$$

where k is a constant equal to 0.9 (for spherical crystallites approximation), λ is a wavelength of X-ray irradiation of Cu Kα, β is the line broadening at half maximum intensity and θ is the Bragg angle. The Williamson – Hall approach was applied to estimate the relative deformations (ε) in the PSi/RuO_2 nanocomposite through the diffraction line broadening, which takes place due to crystallite size, and strain contribution. A typical equation is:[25]

$$\beta\cos\theta = \frac{k\lambda}{D} + 4\varepsilon\sin\theta, \quad (2)$$

Table 2
Estimated values of crystalline size and deformations.

Sample	D ± ΔD (nm)	$\varepsilon \times 10^{-3}$
MOCVD_150	12.6 ± 0.4	5.1
MOCVD_80	8.7 ± 0.9	14.2
MOCVD_60	7.2 ± 0.1	12.3
ALD_50	10 ± 1	33
ALD_90	12.2 ± 0.2	10.9
ALD_130	10.5 ± 0.2	5.6

Table 2 shows calculated values for average nanocrystallites sizes (D) and relative deformations (ε). The average nanocrystallite size is about 11 ± 1 nm for samples obtained by ALD, correlating with TEM results and not significantly depends on the number of ALD cycles. In our previous works, we have shown that the size of nanocrystallites of metal oxide inside the porous matrix is determined by the average size of Si pores [22]. The relative deformations drastically decrease from 3.3×10^{-2} to 5×10^{-3} for 50 and 130 ALD cycles, respectively. This effect is probably relates to the relaxation processes of mechanical stresses which occur at the interface of Si-RuO_2 with increasing the thickness of MOx layer inside PSi matrix. As was previously shown, mechanical stresses accumulating at the interface inside pores depend on the layer thickness and have higher values for thinner layers [26,27]. If this value becomes equal to the threshold stress, the relaxation (deformation) of mechanical stresses occurs, and as a consequence, we observe the decreasing of relative deformations.

Samples obtained by MOCVD method demonstrate other structural and mechanical features. In opposite to ALD technique, the average nanocrystallite size increase with the number of MOCVD injections. The values of relative deformations remain almost the same for all samples produced by MOCVD. These observations can be explained by the fact that the MOCVD RuO_2 layer is mostly distributed in the top of PSi. Therefore, the thickness of the RuO_2 layer are not restricted by the walls of PSi pores, and mechanical stresses/deformations are not affected by the interface effects, as in the case of ALD samples.

In order to confirm the phase of obtained nanocomposites and to detect mechanical effects in the RuO_2 nanocrystals, we have used Raman spectroscopy, due to its high sensitivity to structural deformations [28]. Measured Raman spectra of fabricated MOCVD and ALD nanostructures are shown in Fig. 4. There are the three major Raman modes, E_g, A_{1g} and B_{2g} which are located at ~520, 645 and 715 cm^{-1}, respectively. Last two modes located at 645 and 715 cm^{-1} are less intensive than E_g and not discussed in our research. For samples obtained by both methods, it is clearly seen a Raman peak at around 505 cm^{-1} corresponding to E_g RuO_2 Raman mode. Besides, one can observe an intensive Si mode at 520 cm^{-1} [28]. We can see that the main E_g Raman peak is shifted and broadened in comparison with a single-crystal RuO_2 for samples obtained by MOCVD (Fig. 4a). However, the peak position remains almost the same and do not depend on the number of MOCVD injections. It might be explained by quantum-confinement effect which takes place in RuO_2 layer [28,29]. On the other hand, the E_g peak for samples obtained by ALD shows significant redshift. The possible mechanisms for the peak redshift may result from accumulative effects of quantum confinement and disorder effects induced by grain boundaries or/and by interface strains. Silicon Raman peak located at 520 cm^{-1} also undergoes a certain shift due to mechanical stresses induced by growing of RuO_2 layer inside the PSi matrix. This conclusion is consistent with the XRD results where we have shown that the value of deformations decrease with increasing of the number of ALD cycles. Besides, as was shown in TEM/EDX (Fig. 2d), RuO_2 layer covers the whole area inside the PSi matrix, which induces high values of mechanical stresses. Meanwhile, RuO_2 layer produced by MOCVD mainly deposits the thin top-layer of porous structure and do not effect such significantly on the mechanical stresses.

Additional Raman peaks originated from RuO_2 are located in the

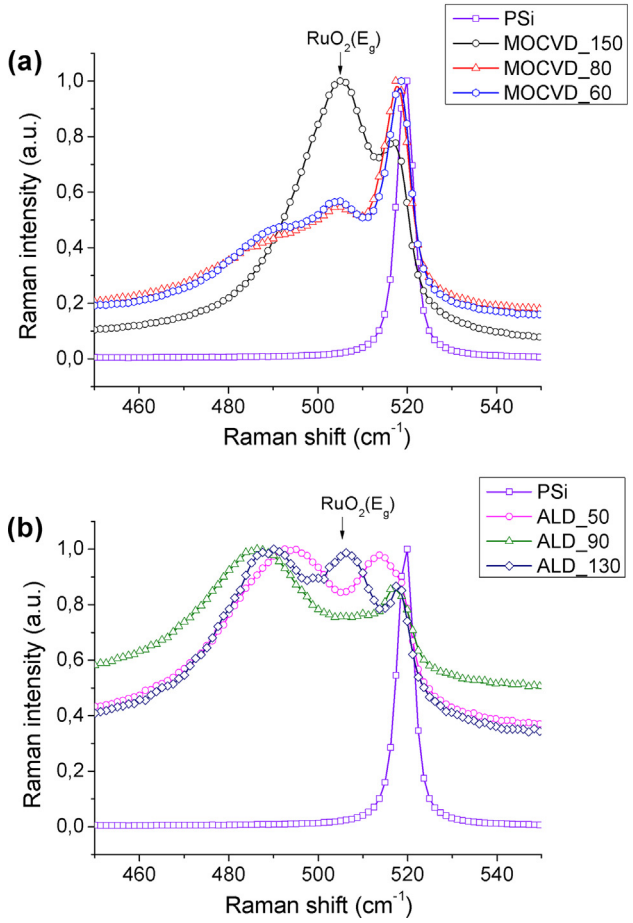

Fig. 4. Raman spectra of MOCVD (a) and ALD (b) PSi/RuO_2 nanostructures.

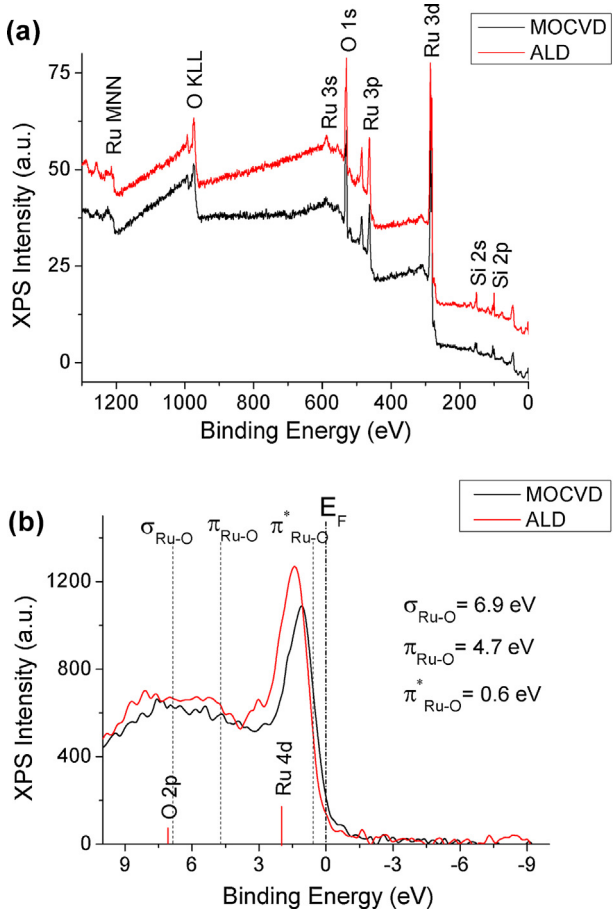

Fig. 5. (a) XPS survey spectra and (b) Valence band spectra of MOCVD and ALD prepared PSi/RuO_2 nanostructures.

range of 480–495 cm^{-1}. According to other researches, this peak can be assigned to the formation of $RuO_2{\cdot}H_2O$ [30,31]. Comparing this peak for both methods, we can observe that the relative intensity for ALD samples is much higher than for samples obtained by MOCVD. We may assume that during ALD processes, the formation of hydrated RuO_2 occurs more intensively because of high ALD precursor reactivity. However, this is still an open question, which requires further investigations.

In order to estimate the average size of RuO_2 nanocrystallites, assuming their spherical shape, we have employed a simple confinement model [29]. The dispersion relation for optical phonons in RuO_2 nanocrystallites was taken from Ref. [29]. The calculated size of RuO_2 nanocrystallites was approximately 4–6 nm, for samples produced by both methods, and did not correspond to the XRD and TEM results because of neglecting mechanical and structural effects in the confinement model.

3.2. XPS analysis

For thorough investigation of oxidation states and chemical composition of fabricated nanocomposites a comprehensive XPS analysis was performed. Measured XPS survey spectra are displayed in Fig. 5a. Both samples produced by ALD and MOCVD depict mainly Ru, O and Si components but also C contaminations. The presence of carbon in samples might be explained by contamination during deposition and etching processes. The high-resolution valence band XPS spectra exhibit two asymmetric features centered at about 2 eV and 7 eV below Fermi Energy (E_F) and attributed to Ru 4d and O 2p, respectively (Fig. 5b). It is known that conductive properties of RuO_2 correlate with the number of free d-electrons [32]. RuO_2 is considered to be metallic-like conductors and electrical conductivity is explained by partially filled metal-oxygen π* band [33]. The Ru 4d and the O 2p levels interact to give metal-oxygen bands with different symmetry σ, π and π*. These orbitals are polarized towards oxygen and lead to peaks $\sigma_{Ru\text{-}O}$, $\pi_{Ru\text{-}O}$ and $\pi^*_{Ru\text{-}O}$ (Fig. 5b). Taking into account that the partially filled $\pi^*_{Ru\text{-}O}$ level is responsible for conductive properties of RuO_2, and comparing XPS intensity at E_F, we can conclude that the samples produced by MOCVD (150 injections) have slightly higher electrical conductivity than ALD (130 cycles) samples. This conclusion was also confirmed by resistance measurements performed by Van der Pauw method for flat samples (SI, Table S2).

The high-resolution XPS core-level spectra for Ru 3d, O 1s and Si 2p and their deconvolution fitting are presented in Fig. 6. The Ru 3d is characterized by two peaks corresponding to the 5/2 and 3/2 spin-orbital components (Fig. 6a and b). Since the C 1s peak coincides with the Ru $3d_{3/2}$ any interpretation of Ru components required careful attention. It is clearly seen two spin-orbital components located at 281.5–285.6 eV and 283.3–287.5 eV, respectively. The value 4.1 eV (285.6–281.5 eV) of spin-orbital splitting is typical for RuO_2 [34]. Second Ru 3d doublet (287.5–283.3 eV), probably originate from hydrated $RuO_2{\cdot}H_2O$. One can also observe C 1s core level peaks of carbon contaminations.

Core-level O 1s spectra for ALD and MOCVD samples are shown in Fig. 6c and d. After deconvolution, the O 1s spectra display three distinct peaks located at 530.0, 532.0 and 533.9 eV for the ALD sample and 530.3, 532.3 and 534.1 eV for the MOCVD sample, which were attributed to the lattice oxygen (O^{2-}) in RuO_2, surface hydroxyl groups (−OH) and the chemisorbed atomic oxygen from hydrated RuO_2, respectively. The third peak at 534 eV could be also attributed to SiO_2.

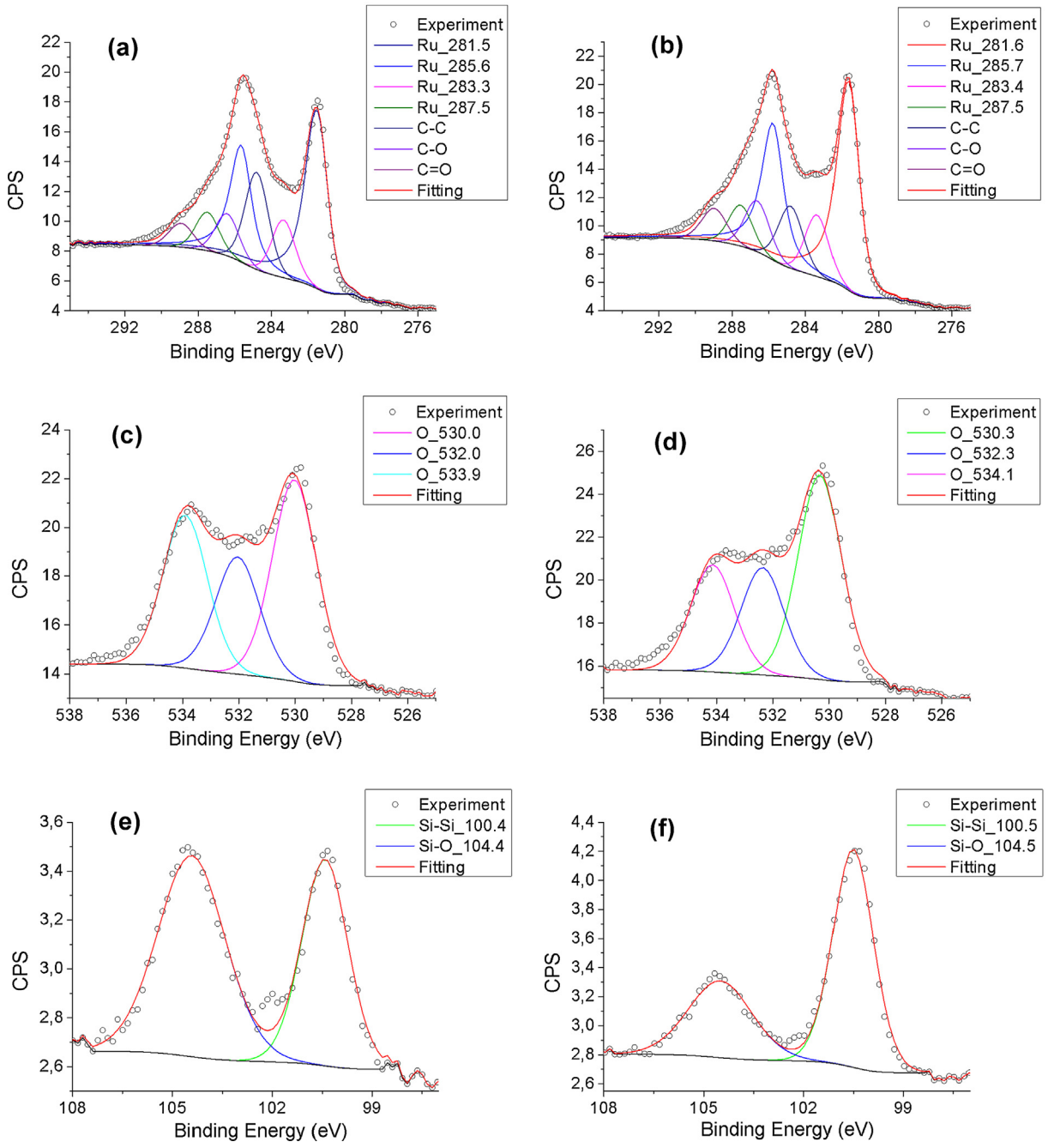

Fig. 6. High-resolution XPS core-level spectra of MOCVD produced samples: (a) Ru 3d, (c) O 1s, (e) Si 2p and ALD produced samples: (b) Ru 3d, (d) O 1s, (f) Si 2p.

The analysis of Si 2p core-level XPS spectra indicates that there are silicon in two states: neutral atoms (Si) with binding energy centered at 100.5 ± 0.2 eV and Si−O bonds with a binding energy of 104.4 ± 0.2 eV (Fig. 5a) [26]. One can notice that the relative concentration of Si-O component for MOCVD sample is much higher than ALD. It may be explained by the enhanced oxidation during MOCVD.

3.3. Optical properties

Finally, to determine optical properties and estimate energy band gap, the samples were investigated by diffusive reflectance and photoluminescence spectroscopy. Fig. 7a shows the diffuse reflectance spectra for MOCVD and ALD samples. It is clearly seen that after MOCVD and/or ALD processes the reflectance in the range 400–800 nm decreased significantly because of high absorption of deposited RuO_2 layer. The average reflectance in the visible range is less than 7%. Increasing of RuO_2 layer thickness leads to decreasing of the total reflectance from 15% (wavelength 700 nm) for MOCVD_60 to less than 10% for MOCVD_150, respectively. The same tendency is observed for samples produced by ALD technique.

In order to estimate the optical band gap (E_g) of RuO_2 in the PSi/RuO_2 nanostructures typical Tauc plots were plotted (Fig. 7b). The band gap values were calculated through Kubelka-Monk formula (4) using the measured diffuse reflectance spectra:[35]

$$F = \frac{(1-R)^2}{2R}, \tag{3}$$

$$(Fhv)^{1/2}\ (hv - E_g), \tag{4}$$

where F, R, hv and E_g represent the Kubelka–Munk function, the diffuse reflectance, photon energy and band gap, respectively. As it is depicted

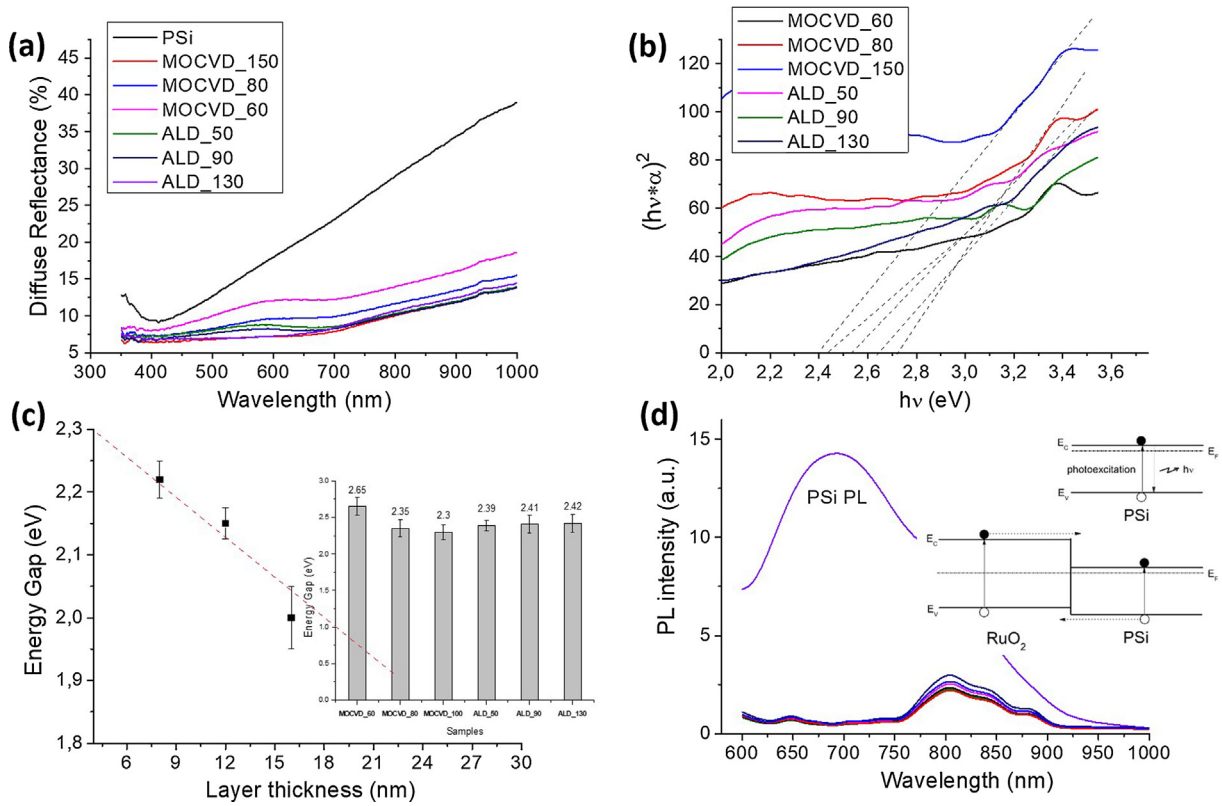

Fig. 7. (a) the diffuse reflectance spectra and (b) Tauc plots for PSi/RuO_2 nanostructures; (c) the band gap energy estimation for RuO_2 layers on glass and (inset) on PSi; (d) PL spectra of PSi/RuO_2 nanostructures and the scheme of quenching mechanism.

in Fig. 7b, the band gap values (E_g) were calculated by intersection of curve's liner parts with the photon energy axis. The average value of E_g for ALD samples was around 2.4 ± 0.1 eV. The obtained E_g values for MOCVD were 2.65 ± 0.3, 2.36 ± 0.2, and 2.30 ± 0.2 eV for 150, 80, and 60 injections, respectively. We have also compared band gap values for RuO_2 layers grown on the flat and PSi surface. Fig. 7c shows estimated band gap values for RuO_2 layers onto glass substrate which were calculated from transmittance spectra (SI, Fig. S3): 2,21 eV, 2,16 eV and 2 eV for 8, 12 and 16 nm respectively. It is clearly seen the gradual decreasing of $E_g$values with increasing the number of MOCVD injections and nonsignificant changes for ALD samples. We suggest that samples with thinner layer (60, 80 MOCVD injections), and as a consequence small size of RuO_2 nanograins, showed higher values of the band gap, which could be related to the quantum confinement effect. The estimated E_g values can also be affected by defects and mechanical stresses [7].

Fig. 7d shows photoluminescence spectra of PSi and RuO_2/PSi nanostructures. Nanolayers of RuO_2, which cover the PSi, may change the surface structure and interface properties, and therefore will lead to significant changes in optical properties of the nanocomposite. The PL peak centered at 700 ± 5 nm (1.77 eV) was observed for PSi. After RuO_2 deposition, the PL peak was almost quenched what indicates that the RuO_2/PSi nanocomposite had a lower recombination rate. We have previously shown that heterojunctions of PSi and metal oxides separate the photogenerated charge carriers due to a difference in the energy levels of their conduction (E_c) and valence (E_v) bands, which improves the photocatalytic activity. The principal scheme of the quenching process is depicted in Fig. 7d (inset).

4. Conclusions

In summary, RuO_2 thin layers on PSi substrate were synthesized using MOCVD and ALD techniques. The crystalline structures, chemical compositions, physical properties of the prepared RuO_2/PSi nanostructures were established, and the main structural (crystalline phase, grain size, layer thickness), optical (band gap energy), and mechanical parameters (deformation) were calculated. Calculated values of deformations remained almost the same for all MOCVD samples, while for ALD samples they drastically changed, showing the influence of layer thickness and RuO_2 distribution in Si pores. The significant Raman spectroscopy peak confirms this conclusion for samples obtained by ALD due to mechanical stresses induced by growing of RuO_2 layer inside the PSi matrix. Mechanical and optical properties of RuO_2/PSi nanostructures are tailored by their structural parameters. The estimated Eg values variations can be related to structural defects, mechanical stresses and to quantum confinement effect. We may conclude that combining the large effective surface area of PSi and the fast charge carrier separation at the RuO_2/PSi heterojunction, provides an opportunity for effective application of RuO_2/PSi nanostructures in photocatalysis and optoelectronics.

Acknowledgment

I.I. acknowledges the financial support from the National Science Centre of Poland by the SONATA 11 project UMO-2016/21/D/ST3/00962.

Appendix A. Supplementary data

Supplementary data to this article can be found online at https://doi.org/10.1016/j.apsusc.2018.12.022.

References

[1] J. Zheng, S. Bao, X. Zhang, H. Wu, R. Chen, P. Jin, Pd-MgNix nanospheres/black-TiO2 porous films with highly efficient hydrogen production by near-complete suppression of surface recombination, Appl. Catal. B Environ. 183 (2016) 69–74,

https://doi.org/10.1016/j.apcatb.2015.10.031.
[2] M. Kan, X. Qian, T. Zhang, D. Yue, Y. Zhao, Highly active IrO_xnanoparticles/black Si electrode for efficient water splitting with conformal TiO_2 interface engineering, ACS Sustain. Chem. Eng. 5 (2017) 10940–10946, https://doi.org/10.1021/acssuschemeng.7b02850.
[3] V. Myndrul, R. Viter, M. Savchuk, N. Shpyrka, D. Erts, D. Jevdokimovs, V. Silamiķelis, V. Smyntyna, A. Ramanavicius, I. Iatsunskyi, Porous silicon based photoluminescence immunosensor for rapid and highly-sensitive detection of Ochratoxin A, Biosens. Bioelectron. 102 (2018) 661–667, https://doi.org/10.1016/j.bios.2017.11.048.
[4] J. Li, M.J. Sailor, Synthesis and characterization of a stable, label-free optical biosensor from TiO2-coated porous silicon, Biosens. Bioelectron. 55 (2014) 372–378, https://doi.org/10.1016/j.bios.2013.12.016.
[5] M. Ge, J. Rong, X. Fang, C. Zhou, Porous doped silicon nanowires for lithium ion battery anode with long cycle life, Nano Lett. 12 (2012) 2318–2323, https://doi.org/10.1021/nl300206e.
[6] S. Sampath, M. Shestakova, P. Maydannik, T. Ivanova, T. Homola, A. Bryukvin, M. Sillanpää, R. Nagumothu, V. Alagan, Photoelectrocatalytic activity of ZnO coated nano-porous silicon by atomic layer deposition, RSC Adv. 6 (2016) 25173–25178, https://doi.org/10.1039/C6RA01655C.
[7] I. Iatsunskyi, M. Pavlenko, R. Viter, M. Jancelewicz, G. Nowaczyk, I. Baleviciute, K. Za, S. Jurga, A. Ramanavicius, V. Smyntyna, Tailoring the structural, optical, and photoluminescence properties of porous silicon/TiO2 nanostructures, J. Phys. Chem. C 119 (2015) 7164–7171, https://doi.org/10.1021/acs.jpcc.5b01670.
[8] M. Pavlenko, E.L. Coy, M. Jancelewicz, K. Zaleski, V. Smyntyna, S. Jurga, I. Iatsunskyi, Enhancement of optical and mechanical properties of Si nanopillars by ALD TiO2 coating, RSC Adv. 6 (2016) 97070–97076, https://doi.org/10.1039/C6RA21742G.
[9] M. Pavlenko, K. Siuzdak, E. Coy, M. Jancelewicz, S. Jurga, I. Iatsunskyi, Silicon/TiO_2 core-shell nanopillar photoanodes for enhanced photoelectrochemical water oxidation, Int. J. Hydrogen Energy 42 (2017) 30076–30085, https://doi.org/10.1016/j.ijhydene.2017.10.033.
[10] P. Dwivedi, S. Dhanekar, S. Das, S. Chandra, Effect of TiO2 functionalization on nano-porous silicon for selective alcohol sensing at room temperature, J. Mater. Sci. Technol. 33 (2017) 516–522, https://doi.org/10.1016/j.jmst.2016.10.010.
[11] M.D. Higham, M. Scharfe, M. Capdevila-Cortada, J. Pérez-Ramírez, N. López, Mechanism of ethylene oxychlorination over ruthenium oxide, J. Catal. 353 (2017) 171–180, https://doi.org/10.1016/j.jcat.2017.07.013.
[12] K.P.J. Gustafson, A. Shatskiy, O. Verho, M.D. Kärkäs, B. Schluschass, C.W. Tai, B. Åkermark, J.E. Bäckvall, E.V. Johnston, Water oxidation mediated by ruthenium oxide nanoparticles supported on siliceous mesocellular foam, Catal. Sci. Technol. 7 (2017) 293–299, https://doi.org/10.1039/c6cy02121b.
[13] M. Mikolasek, K. Frohlich, K. Husekova, J. Racko, V. Rehacek, F. Chymo, M. Tapajna, L. Harmatha, Silicon based MIS photoanode for water oxidation: a comparison of RuO2 and Ni Schottky contacts, Appl. Surf. Sci. 461 (2018) 48–53, https://doi.org/10.1016/J.APSUSC.2018.04.234.
[14] C. Gómez-Solís, J.C. Ballesteros, L.M. Torres-Martínez, I. Juárez-Ramírez, RuO2-NaTaO3 heterostructure for its application in photoelectrochemical water splitting under simulated sunlight illumination, Fuel 166 (2016) 36–41, https://doi.org/10.1016/j.fuel.2015.10.104.
[15] H.G. Jung, Y.S. Jeong, J.B. Park, Y.K. Sun, B. Scrosati, Y.J. Lee, Ruthenium-based electrocatalysts supported on reduced graphene oxide for lithium-air batteries, ACS Nano 7 (2013) 3532–3539, https://doi.org/10.1021/nn400477d.
[16] Y. He, D. Langsdorf, L. Li, H. Over, Versatile model system for studying processes ranging from heterogeneous to photocatalysis: epitaxial RuO2(110) on TiO2(110), J. Phys. Chem. C 119 (2015) 2692–2702, https://doi.org/10.1021/jp5121405.
[17] W. Zheng, Q. Cheng, D. Wang, C.V. Thompson, High-performance solid-state on-chip supercapacitors based on Si nanowires coated with ruthenium oxide via atomic layer deposition, J. Power Sources 341 (2017) 1–10, https://doi.org/10.1016/j.jpowsour.2016.11.093.
[18] K. Hušeková, E. Dobročka, A. Rosová, J. Šoltýs, A. Šatka, F. Fillot, K. Fröhlich, Growth of RuO2 thin films by liquid injection atomic layer deposition, Thin Solid Films 518 (2010) 4701–4704, https://doi.org/10.1016/J.TSF.2009.12.063.
[19] D.-J. Lee, S.-W. Kang, S.-W. Rhee, Chemical vapor deposition of ruthenium oxide thin films from Ru(tmhd)3 using direct liquid injection, Thin Solid Films 413 (2002) 237–242, https://doi.org/10.1016/S0040-6090(02)00439-X.
[20] J.M. Lee, J.C. Shin, C.S. Hwang, H.J. Kim, C.-G. Suk, Preparation of high quality RuO2 electrodes for high dielectric thin films by low pressure metal organic chemical vapor deposition, J. Vac. Sci. Technol., A 16 (1998) 2768–2771, https://doi.org/10.1116/1.581419.
[21] I.-H. Kim, J.-H. Kim, K.-B. Kim, Electrochemical characterization of electrochemically prepared ruthenium oxide/carbon nanotube electrode for supercapacitor application, Electrochem. Solid-State Lett. 8 (2005) A369, https://doi.org/10.1149/1.1925067.
[22] I. Iatsunskyi, M. Jancelewicz, G. Nowaczyk, M. Kempiński, B. Peplińska, M. Jarek, K. Załęski, S. Jurga, V. Smyntyna, Atomic layer deposition TiO2 coated porous silicon surface: structural characterization and morphological features, Thin Solid Films 589 (2015) 303–308, https://doi.org/10.1016/j.tsf.2015.05.056.
[23] L. Liu, X.Q. Bao, Silicon nanowires fabricated by porous gold thin film assisted chemical etching and their photoelectrochemical properties, Mater. Lett. 125 (2014) 28–31, https://doi.org/10.1016/j.matlet.2014.03.145.
[24] A. Ulyanenkov, K. Omote, J. Harada, The genetic algorithm: refinement of X-ray reflectivity data from multilayers and thin films, Phys. BCondens. Matter. 283 (2000) 237–241, https://doi.org/10.1016/S0921-4526(99)01972-9.
[25] P. Bindu, S. Thomas, Estimation of lattice strain in ZnO nanoparticles: X-ray peak profile analysis, J. Theor. Appl. Phys. 8 (2014) 123–134, https://doi.org/10.1007/s40094-014-0141-9.
[26] I. Iatsunskyi, M. Kempiński, G. Nowaczyk, M. Jancelewicz, M. Pavlenko, K. Załeski, S. Jurga, Structural and XPS studies of PSi/TiO2 nanocomposites prepared by ALD and Ag-assisted chemical etching, Appl. Surf. Sci. 347 (2015) 777–783, https://doi.org/10.1016/j.apsusc.2015.04.172.
[27] G. Abadias, E. Chason, J. Keckes, M. Sebastiani, G.B. Thompson, E. Barthel, G.L. Doll, C.E. Murray, C.H. Stoessel, L. Martinu, Review Article: Stress in thin films and coatings: current status, challenges, and prospects, J. Vac. Sci. Technol. A Vacuum, Surfaces, Film. (2018), https://doi.org/10.1116/1.5011790.
[28] I. Iatsunskyi, G. Nowaczyk, S. Jurga, V. Fedorenko, M. Pavlenko, V. Smyntyna, One and two-phonon Raman scattering from nanostructured silicon, Opt. – Int. J. Light Electron Opt. 126 (2015) 1650–1655, https://doi.org/10.1016/j.ijleo.2015.05.088.
[29] S.Y. Mar, C.S. Chen, Y.S. Huang, K.K. Tiong, Characterization of RuO2 thin films by Raman spectroscopy, Appl. Surf. Sci. 90 (1995) 497–504, https://doi.org/10.1016/0169-4332(95)00177-8.
[30] S. Bhaskar, P.S. Dobal, S.B. Majumder, R.S. Katiyar, X-ray photoelectron spectroscopy and micro-Raman analysis of conductive RuO2 thin films, J. Appl. Phys. 89 (2001) 2987–2992, https://doi.org/10.1063/1.1337588.
[31] H.C. Jo, K.M. Kim, H. Cheong, S.-H. Lee, S.K. Deb, In situ raman spectroscopy of RuO·xH2O, Electrochem. Solid-State Lett. 8 (2005) E39, https://doi.org/10.1149/1.1865673.
[32] K. Glassford, J. Chelikowsky, Electronic and structural properties of RuO2, Phys. Rev. B. 47 (1993) 1732–1741, https://doi.org/10.1103/PhysRevB.47.1732.
[33] M. Takeuchi, K. Miwada, H. Nagasaka, Electrical properties of sputtered RuO2 films, Appl. Surf. Sci. 11–12 (1982) 298–307, https://doi.org/10.1016/0378-5963(82)90076-9.
[34] D. Rochefort, P. Dabo, D. Guay, P.M.A. Sherwood, XPS investigations of thermally prepared RuO2 electrodes in reductive conditions, Electrochim. Acta. 48 (2003) 4245–4252, https://doi.org/10.1016/S0013-4686(03)00611-X.
[35] M. Baitimirova, R. Viter, J. Andzane, A. van der Lee, D. Voiry, I. Iatsunskyi, E. Coy, L. Mikoliunaite, S. Tumenas, K. Załęski, Z. Balevicius, I. Baleviciute, A. Ramanaviciene, A. Ramanavicius, S. Jurga, D. Erts, M. Bechelany, Tuning of structural and optical properties of graphene/ZnO nanolaminates, J. Phys. Chem. C 120 (2016) 23716–23725, https://doi.org/10.1021/acs.jpcc.6b07221.